Materials Advances

ROYAL SOCIETY OF CHEMISTRY

PAPER

View Article Online
View Journal | View Issue

Cite this: *Mater. Adv.*, 2026, 7, 1006

Synthesis and characterization of a nanocomposite of an iridium-based complex with mesoporous g-C_3N_4 and its application as a supercapacitor

Mohammad Yaghoubi, [a] Vahid Amani, *[b] Faranak Manteghi *[a] and Edris Jamshidi [a]

The depletion of nonrenewable energy sources and the consequences on the environment brought about by the increase in global energy usage have made energy storage techniques an exceptional option for energy supply. Supercapacitors stand out among them due to their incredible attributes as an electrical energy storage device. Among the three types of materials used in supercapacitors, namely, carbon-based materials, conducting polymers, and transition metal oxides/hydroxides, metal oxides, especially toxic and high-cost oxides, such as RuO_2 and IrO_2, encounter difficulties that restrict their application in supercapacitors, which can be overcome *via* the integration of carbon-based materials that are porous and stable. In this study, we prepared an iridium-based complex and its composite with mesoporous g-C_3N_4, determined their structures, and compared their electrochemical behavior. The structure and morphology of the as-prepared materials were determined by energy-dispersive X-ray (EDX) analysis, X-ray diffraction (XRD) analysis, scanning electron microscopy (SEM) analysis, and Fourier transform infrared (FTIR) spectroscopy. Electrochemical measurements and testing indicated the notable influence of mesoporous g-C_3N_4, improving the specific capacitance from 574 F g^{-1} to 2302 F g^{-1} and energy density from 11.8 Wh kg^{-1} to 47.3 Wh kg^{-1} at a current density of 2 A g^{-1} in [4,4′-dmbipy·H]$_2$[$IrCl_6$] and [4,4′-dmbipy·H]$_2$[$IrCl_6$]@mesoporous g-C_3N_4, respectively. Additionally, [4,4′-dmbipy·H]$_2$[$IrCl_6$] showed a 99.27% Coulombic efficiency after 5000 cycles at a current density of 8 A g^{-1}, which increased to a notable 100.46% Coulombic efficiency after 5000 cycles at a high current density of 20 A g^{-1}.

Received 29th August 2025,
Accepted 24th November 2025

DOI: 10.1039/d5ma00981b

rsc.li/materials-advances

1. Introduction

Due to the prediction of increased energy consumption by roughly 50% by 2040 and the doubling of the global energy usage in the last half-century, two issues will arise, namely, resource exhaustion in about 100 years and the increased health and environmental effects of contaminants and greenhouse gases, because the world's electrical energy supply is overly dependent on nonrenewable resources like coal, gas, and fuels. Since the 20th century, renewable sources, such as biomass, solar, wind, and hydropower, have become suitable substitutes for supplying the world's required energy and reducing the greenhouse gases.[1–3] Growth in production and demand has led to changes in energy storage methods, with new devices replacing older devices that generally used supercapacitors and batteries for energy storage applications; batteries are used in long-life devices and supercapacitors in fast-charging and fast-discharging devices.[4–6] Among these energy storage devices, the environmental benefits of supercapacitors have drawn a lot of interest. Instead of a solid dielectric utilized in batteries to increase the speed of charging cycles, provide high capacitance values and high power densities, operate in different temperature ranges, improve durability, and offer higher efficiency, supercapacitors employ electrical double-layer capacitance and pseudocapacitance.[7,8] Because of their remarkable properties, they are promising, smart, and flexible energy storage devices with the advantages of high power and energy densities, superfast charge/discharge performance, and good stability, resulting in their various applications in electrical devices.[9,10] Achieving a high-performance supercapacitor will be actualized by developing an ecofriendly and high-conductivity electrode material that operates stably at high

[a] *Research Laboratory of Inorganic Chemistry and Environment, Department of Chemistry, Iran University of Science and Technology, 16846-13114 Tehran, Iran. E-mail: f_manteghi@iust.ac.ir*
[b] *Department of Chemistry Education, Farhangian University, P.O. Box 14665-889, Tehran, Iran. E-mail: v.amani@cfu.ac.ir*

temperatures and has a large specific area and low cost. Porosity directly affects SC devices by increasing their surface area, specific energy, and specific capacitance because porous materials have active sites for adsorption and desorption, in addition to ion and electron transportation.[11,12] Four types of multidimensional (zero-, one-, two-, and three-dimensional) active materials have been applied as supercapacitor materials due to their recent popularity: (a) carbon-based materials, (b) conducting polymers, and (c) transition metal oxides/hydroxides, along with various composites of these groups[11–14] Among the several electrode materials used in SC applications, metal oxides exhibit significant performance as pseudocapacitance materials due to their high capacity and energy capability. Iridium oxide, IrO_2 exhibits the remarkable pseudocapacitance features of iridium. Furthermore, it introduces interesting characteristics like different oxidation states, metal-like conductivity, a wide range of potential windows, stability in basic or acidic solutions, thermal stability, exceptional surface area, and high capacity for the charging process.[15–20] Even though the metal oxides are notable materials for SC electrodes with unique features, they struggle major challenges like their non-movable and non-generatable pores, high cost, toxicity, sheet and charge transfer resistance caused by low conductivity, as well as unacceptable surface area, stability drawbacks, changing volume during reactions, lack of performance in the pristine form, low-term cyclic duration for electrochemical redox reactions, dendrite growth, and high dependence on the electrolyte.[16,20–24] These challenges primarily affect IrO_2 and RuO_2 due to the high cost and toxicity associated with these oxides, which can be improved through integration and composition strategies with nanostructures or carbon-based materials.[16,22] Meanwhile, popular electrode materials based on carbon materials include carbon dots, carbon quantum dots, the graphene-based materials, carbon nanotubes, carbon fibers, carbon nanofibers, and activated carbon, which are capable of combining with different structures by constructing potent covalent bonds to form new compositions with great strength, density, and hardness in various shapes such as powders, nanotubes, fibers, foils, and composites.[25–27] Electrodes made by carbon-based materials are porous, stable, tunable, and adaptive. They are introduced as a high-performance nominee for energy storage process, especially in supercapacitor devices, for their fantastic physiochemical features like high conductivity and high specific surface area, long cyclic durability, thermal and chemical stability, besides their defected sites for heteroatoms.[28–30] Meanwhile, among carbon allotropes, especially effective carbon nanomaterials for energy storage systems, graphitic carbon nitride (g-C_3N_4), a graphene-like 2D metal-free structure with a controllable and tunable morphology, has become a promising electrode material for energy storage devices due to its tremendous physicochemical features, like providing electrochemical performance enhancement in composites due to the appearance of nonbonded electron pairs at nitrogen sites.[31–33] Furthermore, g-C_3N_4 showing physicochemical and structural properties like high durability in mechanical and chemical situations, π-conjugated bonding, and high specific surface area emerged as a high-performance alternative to conventional carbon-based electrode materials such as carbon nanotubes, graphene, and activated carbon.[34–36] As a research background for g-C_3N_4 composites, Khasim *et al.* developed a metal oxide nanocomposite as a supercapacitor electrode material. They checked the electrochemical behavior of the g-C_3N_4/CuO nanocomposite in 6 M KOH using Ag/AgCl as a counter electrode. The as-prepared composite exhibited a specific capacitance of 248 F g^{-1} at a current density of 2 A g^{-1} and a 96% Coulombic efficiency stability after 5000 cycles, along with energy and power densities of 73 Wh kg^{-1} and 1662 kW kg^{-1}, respectively.[37] Also, Zahra *et al.* prepared V_2O_5@g-CN by the hydrothermal method, and their electrochemical research was performed in 2 M KOH using Ag/AgCl as a reference electrode. The specific capacitance of the as-prepared composite was 994 F g^{-1} at a current density of 2 A g^{-1}, while the sample exhibited a 138 Wh kg^{-1} energy density at a 791 W kg^{-1} power density, with remarkable stability after 5000 cycles.[38] However, there is no research on the use of transition metal complexes in SCs to date. The considerable electrochemical features of pyridine-based iridium complexes, such as reversible performance in electrochemical operations, ease of synthesis, tunable structures, and fantastic stability in redox reactions for ionic iridium-based complexes, widen their applications in the field of electrochemistry, such as photoredox catalysis, visible light water splitting, and dye-sensitized solar cells.[39,40] In this work, we prepared a complex using iridium (Ir) as a metal and bipyridine as a ligand and composited it with mesoporous g-C_3N_4 for supercapacitor applications. The morphological and structural analyses of the as-prepared complex and composite were done. Meanwhile, their electrochemical behavior was studied in a 6 M KOH solution.

2. Experimental

2.1. Materials

Hydrochloric acid, ethanol, *N*-methyl-2-pyrrolidone (NMP), activated carbon, polytetrafluoroethylene (PTFE), urea, melamine, hydrogen hexachloroiridate(IV) hydrate, 4,4′-dimethyl-2,2′-bipyridine, and nickel foam sheets were purchased from Sigma Aldrich, and no additional purification was performed.

2.2. Synthesis of mesoporous g-C_3N_4

A mixture of melamine and urea at a molar ratio of 1 : 12 (3 g of melamine and 14 g of urea) was used. The mixture was heated twice using different temperature programs. First, the mixture was heated for 30 minutes at 180 °C at a heating rate of 3 °C min^{-1}; then, at the same heating rate, it was heated at 550 °C for 2 h. After heating at 60 °C for 24 h in a vacuum oven, the final yellow powder obtained was mesoporous g-C_3N_4.[41]

2.3. Synthesis of [4,4′-dmbipy·H]$_2$[IrCl$_6$] (1)

A solution of the 4,4′-dimethyl-2,2′-bipyridine ligand (0.22 g, 1.2 mmol) in ethanol (8 mL) was added to a solution of $H_2IrCl_6 \cdot H_2O$ (0.25 g, 0.6 mmol) in ethanol (8 mL). The mixture was stirred for 15 min at 45 °C to obtain a brown precipitate. The

brown precipitate was collected by filtration and washed several times with ethanol to remove any unreacted free ligand and salt (yield = 0.42 g, relative to $H_2IrCl_6{\cdot}H_2O$, 90.3%; m.p. 232 °C). Elemental analysis calc: C, 37.17; H, 3.35; N, 7.22. Exp: C, 37.02; H, 3.33; N, 7.16.

2.4. Synthesis of [4,4′-dmbipy·H]$_2$[IrCl$_6$]·2DMSO (2)

To investigate the exact structure of complex **1**, this compound was recrystallized in a dimethyl sulfide solvent. The brown block single crystals of **2** suitable for X-ray analyses were obtained by ethanol diffusion of a brown solution of complex **1** in dimethyl sulfide over two weeks. Elemental analysis calc: C, 36.09; H, 4.08; N, 6.01; S, 6.87. Exp: C, 35.92; H, 4.06; N, 5.96; S, 6.81.

2.5. Synthesis of [4,4′-dmbipy·H]$_2$[IrCl$_6$]@mesoporous g-C_3N_4

The as-prepared powder of mesoporous g-C_3N_4 (0.1 g) was added to a solution of the 4,4′-dimethyl-2,2′-bipyridine ligand (0.1 g) in ethanol and sonicated at 50 °C for 20 minutes. Finally, a solution of $H_2IrCl_6{\cdot}H_2O$ (0.1 g) in ethanol was added to the mixture, and the composite ([4,4′-dmbipy·H]$_2$[IrCl$_6$]@mesoporous g-C_3N_4) was obtained after heating at 60 °C for 24 h in a vacuum oven.

2.6. Structural analysis

The morphology and structure were investigated by energy-dispersive X-ray analysis (EDX), X-ray diffraction analysis (XRD), scanning electron microscopy analysis (SEM), and Fourier transform infrared (FTIR) spectroscopy.

2.7. Electrochemical analysis

Each prepared sample's electrochemical behavior was examined by cyclic voltammetry (CV), galvanostatic charge–discharge (GCD), and electrochemical impedance spectroscopy (EIS) in a three-electrode system using Ag/AgCl as the reference electrode and a platinum electrode as the counter electrode in an aqueous solution of 6 M KOH, and the rest of the electrochemical calculations were performed.

2.8. Electrode preparation and electrochemical characterizations

All samples (mesoporous g-C_3N_4, [4,4′-dmbipy·H]$_2$[IrCl$_6$], and [4,4′-dmbipy·H]$_2$[IrCl$_6$]@mesoporous g-C_3N_4) were fabricated by drop-casting the NMP solvent-based mixture of working materials, PTFE, and activated carbon with the molar ratio of 80 : 10:10 on a 1 × 1 cm^2 nickel foam, with about 1.0 mg cm^{-2} mass loading for all work electrodes. Work electrodes were dried in a vacuum oven at 65 °C for 24 h. All the measurements were done in an asymmetric three-electrode system comprising Ag/AgCl as the reference electrode, platinum as the counter electrode, and the prepared electrode materials as the working electrode in a 6 M KOH electrolyte. Cyclic voltammetry (CV), galvanostatic charge–discharge (GCD) measurements, and electrochemical impedance spectroscopy (EIS) measurements were carried out using an electrochemical workstation (Autolab model: PGSTAT204). The specific capacitance (C_s, F g^{-1}), energy density (E_d, Wh kg^{-1}), and power density (P_d, W kg^{-1}) were calculated by eqn (1), (2), and (3), respectively, from GCD results.[42,43]

$$C_s = \frac{I \times \Delta t}{m \times \Delta V} \quad (1)$$

where I (A), Δt (s), m (g), and ΔV (V) are the charge/discharge current, discharge time, total mass of the electrode material, and potential window, respectively.

$$E_d = \frac{1}{7.2} C_s V^2 \quad (2)$$

where C_s is the specific capacitance (F g^{-1}) and V represents the potential window (V).

$$P_d = \frac{E_d}{t} \times 3600 \quad (3)$$

E_d is the energy density (Wh kg^{-1}) and t is the discharge time (s).

3. Results and discussion

3.1. Morphological and structural analysis

The X-ray diffraction measurements for the title complex were performed on a Bruker APEX II CCD area detector diffractometer (Mo Kα radiation, graphite monochromator, λ = 0.71073 Å) at 298 K. The structure of complex **1** was solved by SHELX-97, and absorption correction was done using the SADABS programs.[42,43] Data collection, cell refinement, and data reduction were performed by APEX II, SAINT, SHELXTL, and PLATON.[43–46] The molecular graphic was generated using the Mercury 2.4 program.[47,48]

3.1.1. Materials and physical methods. All chemicals were purchased from Sigma Aldrich. Elemental analysis was performed using a Heraeus CHN–O rapid analyzer. Melting points were obtained on a Kofler Heizbank Rechart type 7841 melting point apparatus.

3.1.2. Description of the molecular structure of 2. The crystallographic data for [4,4′-dmbipy·H]$_2$[IrCl$_6$]·2DMSO (**2**) are given in Table 1, and selected bond lengths and angles are presented in Table 2. This complex crystallizes in the triclinic crystal system with the $P\bar{1}$ space group. The molecular structure of the title complex, together with the atomic labeling scheme, is shown in Fig. 1. As shown in this figure, the asymmetric unit of **2** contains one independent protonated 4,4′-dimethyl-2,2′-bipyridinium (4,4′-dmbipy·H) cation, one half of a $[IrCl_6]^{2-}$ anion, and one dimethyl sulfoxide solvate. It is notable that in the dimethyl sulfoxide solvent, according to high thermal motions of the sulfur atom, this atom is refined in two positions with a reduced occupancy. In the $[IrCl_6]^{2-}$ anion, the Ir(IV) cation has an octahedral coordination by six terminal Cl atoms. The Ir–Cl bond lengths are in the range of 2.312(18)–2.3283(18) Å (Table 2). The Cl1^i–Ir1–Cl1, Cl2^i–Ir1–Cl2, and Cl3^i–Ir1–Cl3 (i is $-x$, $-y$ + 1, $-z$ + 2)

Table 1 Crystallographic and structural refinement data for **2**

Formula	$C_{28}H_{38}Cl_6Ir_1N_4O_2S_2$
Formula weight	931.68
Temperature/K	298(2)
Wavelength λ/Å	0.71073
Crystal system	Triclinic
Space group	$P\bar{1}$
Crystal size/mm	0.50 × 0.45 × 0.25
a/Å	8.3828(6)
b/Å	9.3867(7)
c/Å	12.2743(8)
α/°	87.874(5)
β/°	75.486(5)
γ/°	72.832(6)
Volume/Å^3	892.63(11)
Z	1
Density (calc.)/g cm^{-1}	1.733
θ ranges for data collection	2.63–27.00
F(000)	461
Absorption coefficient	4.338
Index ranges	$-10 \le h \le 10$ $-11 \le k \le 11$ $-15 \le l \le 15$
Data collected	8117
Unique data (R_{int})	3870, 0.1281
Parameters, restrains	208, 0
Final R_1, wR_2 (Obs. data)	0.0468, 0.1242
Final R_1, wR_2 (All data)	0.0468, 0.1242
Goodness of fit on F^2 (S)	1.036
Largest diff. peak and hole/e Å^{-3}	2.322, −3.191
CCDC no.	2453322

Table 2 Selected bond lengths (Å) and angles (°) for **2**

Ir1–Cl1	2.3124(18)	Cl1–Ir1–Cl3^i	90.73(10)
Ir1–Cl2	2.3243(18)	Cl2–Ir1–Cl3^i	90.07(8)
Ir1–Cl3	2.3283(18)	Cl1–Ir1–Cl3	89.27(10)
Cl1^i–Ir1–Cl1	180.0	Cl2^i–Ir1–Cl3	90.07(8)
Cl1–Ir1–Cl2^i	89.40(9)	Cl2–Ir1–Cl3	89.93(8)
Cl1–Ir1–Cl2	90.60(9)	Cl3^i–Ir1–Cl3	180.0
Cl2^i–Ir1–Cl2	180.0		

Symmetry code: (i) $-x$, $-y+1$, $-z+2$.

bond angles are 180.0°, which shows that the structure of this anionic complex is regular octahedral. The Ir–Cl bond lengths and bond angles are in good agreement with the corresponding values in $[en{\cdot}H_2][IrCl_6]$[49] and $[NBu_4]_2[IrCl_6]$.[50]

The crystal packing diagram for **2** is shown in Fig. 2. As shown in this figure, intra- and inter-molecular N–H···O, C–H···O, N–H···S and C–H···Cl hydrogen bonds (Table 3) and π···π interactions between the pyridine rings and Cg1···Cg2^{iii} [the centroid-to-centroid distance is 3.740(4) Å; the symmetry code is $-x$, $-y$, $1-z$; and Cg1 and Cg2 are the centroid of the rings (N1/C1–C3/C5/C6) and (N2/C7–C9/C11/C12), respectively] lead to the formation of a three-dimensional supramolecular network.

Scanning electron microscopy (SEM) analysis (Fig. 3) and energy-dispersive X-ray spectroscopy (EDS) and elemental mapping (Fig. 4) were employed to examine the distribution of constituents and the morphology of the prepared materials, respectively. The SEM images of mesoporous g-C_3N_4 (Fig. 3a) indicate a spherical morphology with the particle size distribution ranging from 101.6 to 207.3 nm. Although the SEM images of $[4,4'\text{-dmbipy}{\cdot}H]_2[IrCl_6]$ (Fig. 3b) show no regular morphology, in $[4,4'\text{-dmbipy}{\cdot}H]_2[IrCl_6]$@mesoporous g-$C_3N_4$ (Fig. 3c), mesoporous g-C_3N_4 is uniformly present, with a particle size distribution between 106.8 and 159.8 nm. The nanostructure and porosity of mesoporous g-C_3N_4 improve the electrochemical performance of $[4,4'\text{-dmbipy}{\cdot}H]_2[IrCl_6]$ by increasing the specific surface area and providing nanopores for electron trapping to facilitate the redox reactions. The EDS spectra and elemental mappings of mesoporous g-C_3N_4 (Fig. 4a), $[4,4'\text{-dmbipy}{\cdot}H]_2[IrCl_6]$ (Fig. 4b) and $[4,4'\text{-dmbipy}{\cdot}H]_2[IrCl_6]$@mesoporous g-$C_3N_4$ (Fig. 4c) show the atomic percentages of 46.02% C and 53.96% N for mesoporous g-C_3N_4, 63.35% C, 25.50% N, 10.10% Cl and 1.04% Ir for $[4,4'\text{-dmbipy}{\cdot}H]_2[IrCl_6]$ and 51.53% C, 37.51% N, 2.31% O, 2.31% Cl and 0.44% Ir for

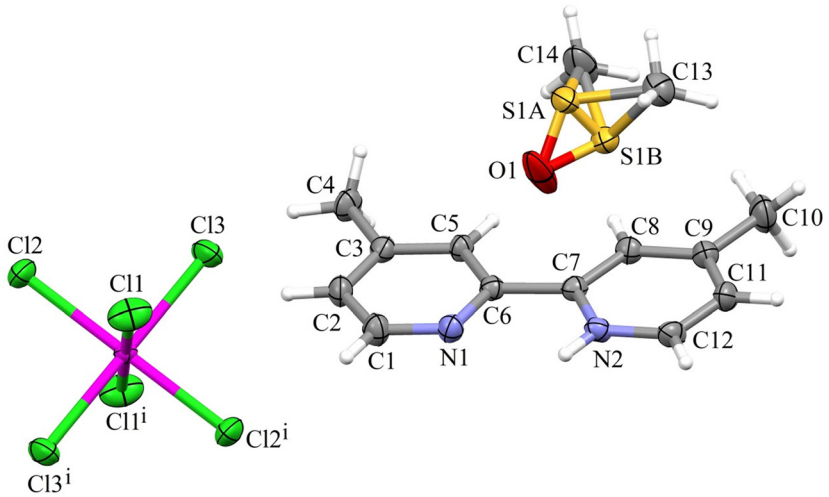

Fig. 1 Molecular structure of $[4,4'\text{-dmbipy}{\cdot}H]_2[IrCl_6]{\cdot}2DMSO$ (**2**) with 30% probability displacement ellipsoids and atom-numbering scheme. Symmetry code: (i) $-x$, $-y+1$, $-z+2$.

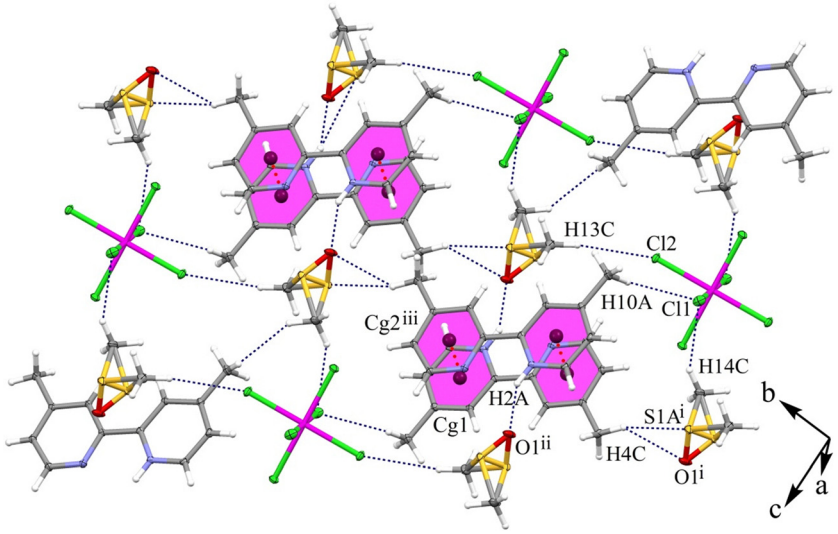

Fig. 2 Crystal packing diagram for $[4,4'\text{-dmbipy}\cdot H]_2[IrCl_6]\cdot 2DMSO$ (**2**). Intra- and inter-molecular N–H···O, C–H···O, N–H···S, and C–H···Cl hydrogen bonds and π···π interactions are shown as dashed lines. Symmetry codes: (i) $-x, 1-y, 1-z$, (ii) $1-x, -y, 1-z$ and (iii) $-x, -y, 1-z$.

Table 3 Hydrogen bond geometry for **2** in the crystal packing

D–H···A	D–H/Å	H···A/Å	D···A/Å	D–H···A/°	Symmetry code
N2–H2A···O1	0.860	1.920	2.685(10)	148	$1-x, -y, 1-z$
C4–H4C···O1	0.960	2.720	3.50(1)	139	$-x, 1-y, 1-z$
C4–H4C···S	0.960	2.889	3.787(8)	156	$-x, 1-y, 1-z$
C13–H13C···Cl2	0.960	2.869	3.81(1)	168	—
C10–H110A···Cl1	0.960	2.886	3.81(1)	163	—
C14–H14C···Cl1	0.960	2.877	3.48(1)	122	—

$[4,4'\text{-dmbipy}\cdot H]_2[IrCl_6]$@mesoporous g-$C_3N_4$, which correctly confirms the amount of materials used in the synthesis. It is crucial to keep in mind that the increase in N in $[4,4'\text{-dmbipy}\cdot H]_2[IrCl_6]$@mesoporous g-$C_3N_4$ is related to the presence of mesoporous g-C_3N_4 in the composite.

Fig. 5 illustrates the Fourier transform infrared (FTIR) spectroscopy data, which were obtained to confirm the successful synthesis and identify the functional groups in the materials synthesized. In the FT-IR spectrum of mesoporous g-C_3N_4, the sharp peak at 814 cm^{-1} is attributed to the heptazine ring. The N–H bending vibration is observed at 885 cm^{-1}. The two peaks at 1246 and 1324 cm^{-1} refer to the aromatic C–N stretching vibration, and the group of peaks in the range from 1420 cm^{-1} to 1642 cm^{-1} can be related to the C=C tensile vibration.[44–46] For $[4,4'\text{-dmbipy}\cdot H]_2[IrCl_6]$, the peak at 826 cm^{-1}, the group of peaks in the range from 1226 to 1596 cm^{-1}, and the peak at 3089 cm^{-1} can be related to the 4,4′-dimethyl-2,2′-bipyridine aromatic ring, C=C tensile vibration, and C–H stretching vibration, respectively. Lastly, the composite's successful synthesis is demonstrated by the complex and mesoporous g-C_3N_4 peaks that are visible in the composite's ($[4,4'\text{-dmbipy}\cdot H]_2[IrCl_6]$@mesoporous g-$C_3N_4$'s) spectrum. Notably, the solvent's hydroxyl (–OH) groups are the cause of the broad peak that is visible at about 3400 cm^{-1} for all as-prepared compounds.[47–52]

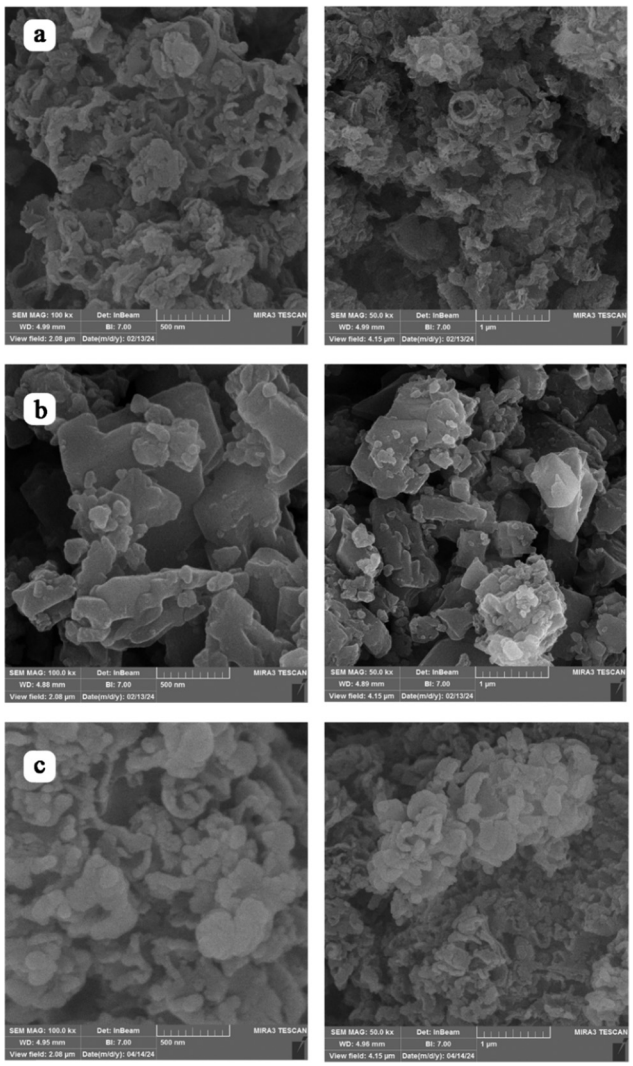

Fig. 3 SEM images of mesoporous g-C_3N_4 (a), $[4,4'\text{-dmbipy}\cdot H]_2[IrCl_6]$ (b) and $[4,4'\text{-dmbipy}\cdot H]_2[IrCl_6]$@mesoporous g-$C_3N_4$ (c).

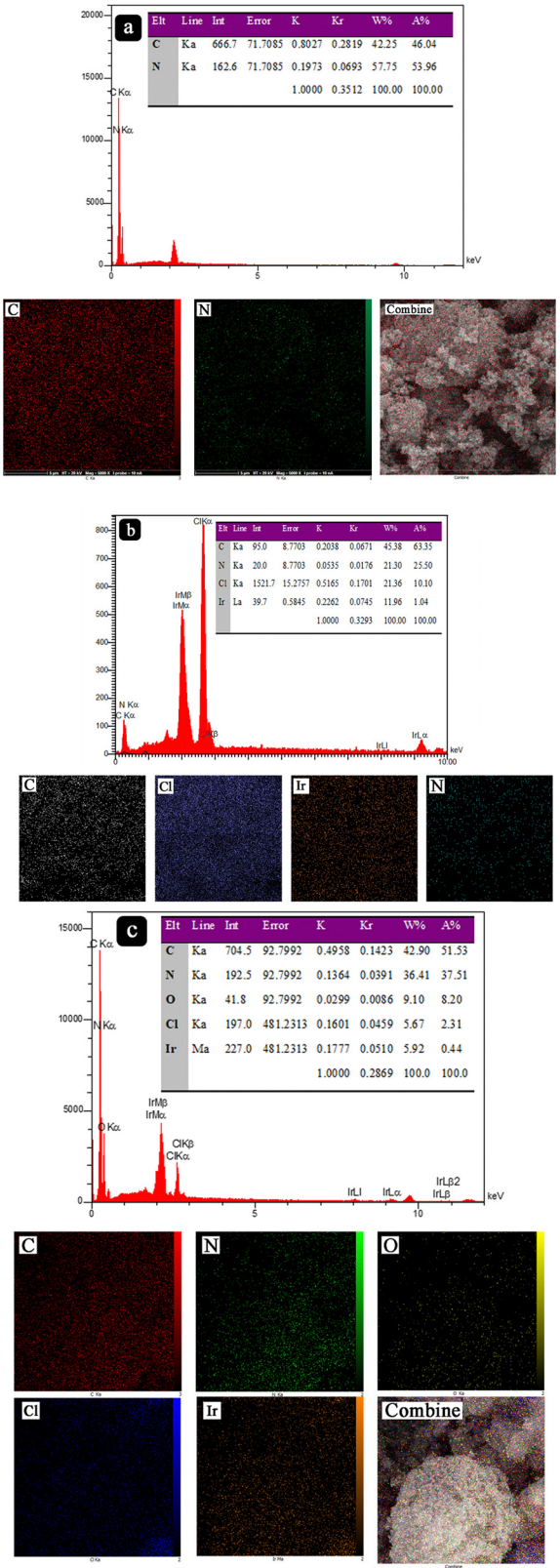

Fig. 4 EDS and elemental mapping images of mesoporous g-C_3N_4 (a), $[4,4'\text{-dmbipy}\cdot H]_2[IrCl_6]$ (b) and $[4,4'\text{-dmbipy}\cdot H]_2[IrCl_6]$@mesoporous g-$C_3N_4$ (c).

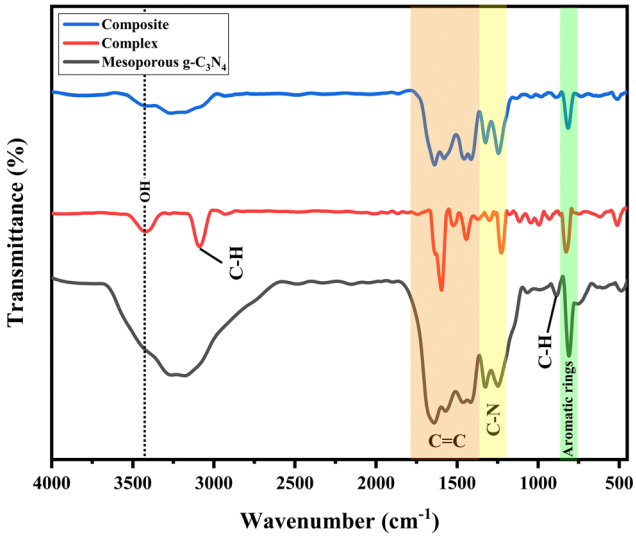

Fig. 5 FTIR spectra of mesoporous g-C_3N_4, $[4,4'\text{-dmbipy}\cdot H]_2[IrCl_6]$ and $[4,4'\text{-dmbipy}\cdot H]_2[IrCl_6]$@mesoporous g-$C_3N_4$.

Fig. 6 displays the X-ray diffraction (XRD) patterns of the as-prepared materials, which were used to identify phases and define crystal structures. In the red pattern, which refers to $[4,4'\text{-dmbipy}\cdot H]_2[IrCl_6]$, the peaks at 2θ of 9.16°, 11.52°, 12.28°, 13.08°, 14.92°, 17°, 18.32°, 20.24°, 21.04°, and 27.92° are related to (010), (100), (0$\bar{1}$0), (111), (002), ($\bar{1}$10), (012), (120), ($\bar{1}$02) and (203), respectively, obtained from the CIF file of $[4,4'\text{-dmbipy}\cdot H]_2[IrCl_6]\cdot 2DMSO$ with mercury 1.4.2 software. For mesoporous g-C_3N_4, the green pattern indicates two main peaks at 2θ of 13.24° and 27.64° for (100) and (002) planes, respectively, which corresponded to JCPDS no. 87-1526. In the blue pattern, which refers to $[4,4'\text{-dmbipy}\cdot H]_2[IrCl_6]$@mesoporous g-$C_3N_4$, mesoporous g-$C_3N_4$ planes appear at 2θ of 13.08° and 27.56° for

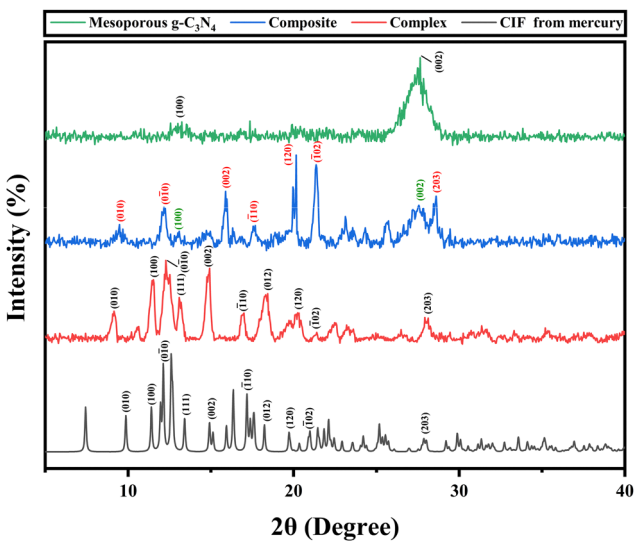

Fig. 6 XRD plots of mesoporous g-C_3N_4 (green), $[4,4'\text{-dmbipy}\cdot H]_2[IrCl_6]$ (red), and $[4,4'\text{-dmbipy}\cdot H]_2[IrCl_6]$@mesoporous g-$C_3N_4$ (blue), and a simulation of $[4,4'\text{-dmbipy}\cdot H]_2[IrCl_6]\cdot 2DMSO$ (black).

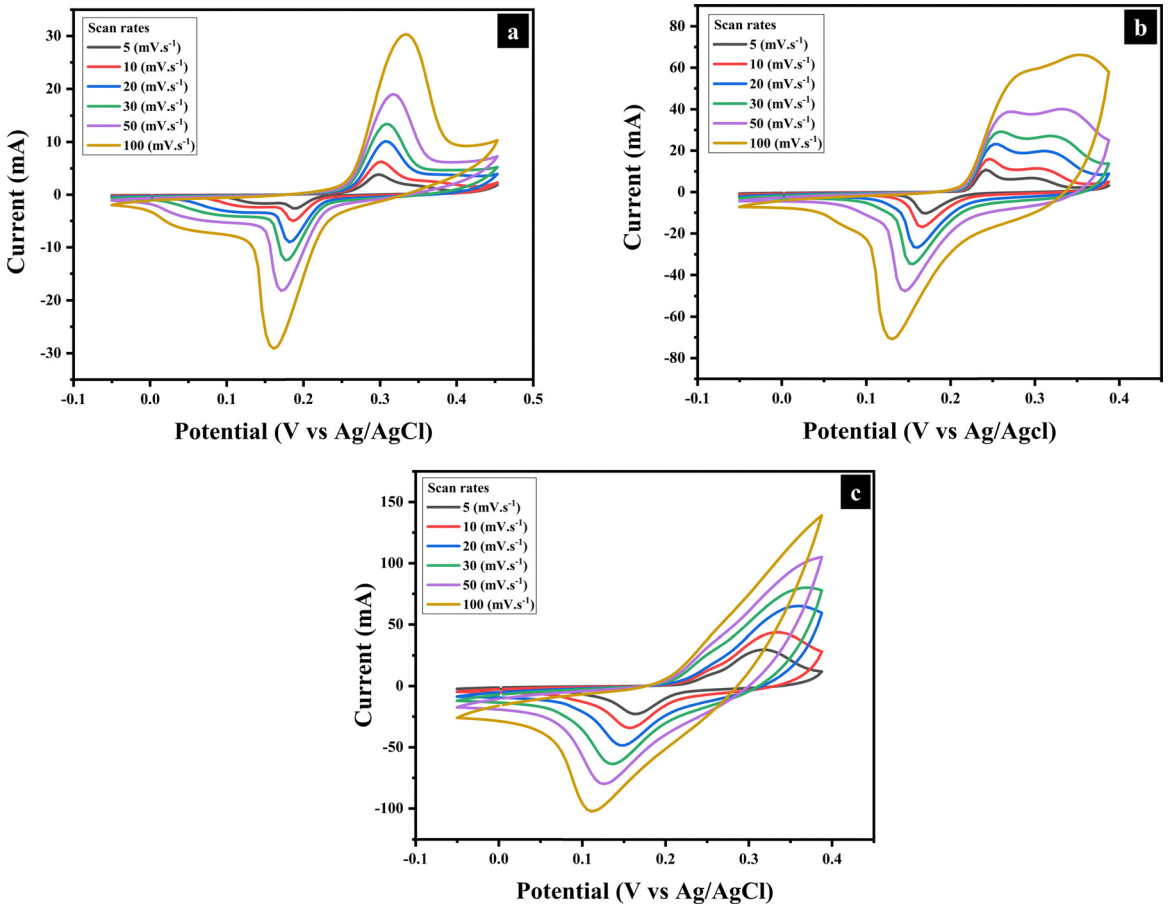

Fig. 7 CV curves of mesoporous g-C_3N_4 (a), [4,4′-dmbipy·H]$_2$[$IrCl_6$] (b) and [4,4′-dmbipy·H]$_2$[$IrCl_6$]@mesoporous g-C_3N_4 (c).

(100) and (002), respectively. The [4,4′-dmbipy·H]$_2$[$IrCl_6$] peaks in the composite are seen at 2θ of 9.48°, 12.16°, 15.88°, 17.68°, 20.16°, 21.36°, and 28.6°, which refer to (010), (0$\bar{1}$0), (002), ($\bar{1}$10), (120), ($\bar{1}$02), and (203) planes, respectively, among which (0$\bar{1}$0) and ($\bar{1}$10) are the outcomes of the overlapping of (100), (0$\bar{1}$0), and (111) planes and ($\bar{1}$. 10) and (012) planes, respectively.

3.2. Electrochemical analysis

The experiments using cyclic voltammetry (CV) were conducted at scan rates of 5, 10, 20, 30, 50, and 100 mV s^{-1} in the potential range from 0.0 V to 0.44 V for g-C_3N_4 and 0.0 V to 0.385 V for [4,4′-dmbipy·H]$_2$[$IrCl_6$] and [4,4′-dmbipy·H]$_2$[$IrCl_6$]@mesoporous g-C_3N_4. Fig. 7 shows the CV curves of mesoporous g-C_3N_4 (a), [4,4′-dmbipy·H]$_2$[$IrCl_6$] (b), and [4,4′-dmbipy·H]$_2$[$IrCl_6$]@mesoporous g-C_3N_4 (c). As expected from a carbon-based material, mesoporous g-C_3N_4 had a semisymmetric CV curve. Furthermore, the asymmetric CV curves of [4,4′-dmbipy·H]$_2$[$IrCl_6$] and [4,4′-dmbipy·H]$_2$[$IrCl_6$]@mesoporous g-C_3N_4 could be related to the battery-type behavior of the as-prepared materials.[53] The wider potential window of [4,4′-dmbipy·H]$_2$[$IrCl_6$]@mesoporous g-C_3N_4 than [4,4′-dmbipy·H]$_2$[$IrCl_6$] noted the beneficial effects of mesoporous g-C_3N_4 on the redox reactions of [4,4′-dmbipy·H]$_2$[$IrCl_6$] in the composite. The double-peaked points in the CV curve of [4,4′-dmbipy·H]$_2$[$IrCl_6$], which can be seen in the CV curve of [4,4′-dmbipy·H]$_2$[$IrCl_6$]@mesoporous g-C_3N_4 at the lowest scan rates, might be connected to iridium's many oxidation states.

The galvanostatic charge–discharge (GCD) tests were carried out at current densities of 2, 3, 5, and 6 A g^{-1} for each of the three produced materials in the same potential window as CV curves to evaluate both charge–discharge performance and electrochemical calculations from eqn (1)–(3). Fig. 8 shows the GCD plots of mesoporous g-C_3N_4 (a), [4,4′-dmbipy·H]$_2$[$IrCl_6$] (b), and [4,4′-dmbipy·H]$_2$[$IrCl_6$]@mesoporous g-C_3N_4 (c).

The composite showed an increase in charge and especially discharge time, compared to the complex. which efficiently impacted the specific capacitance (C_s), energy density (E_d), and power density (P_d), according to eqn (1)–(3). Mesoporous g-C_3N_4 achieved C_s of 88, 95, 101, 111, and 125 F g^{-1} at current densities of 6, 5, 4, 3, and 2 A g^{-1}, respectively. Meanwhile, the specific capacitances of [4,4′-dmbipy·H]$_2$[$IrCl_6$] at current densities of 6, 5, 4, 3, and 2 A g^{-1} were 389, 427, 449, 505, and 574 F g^{-1}, which impressively increased to 1807, 1920, 2015, 2124, and 2302 F g^{-1} for [4,4′-dmbipy·H]$_2$[$IrCl_6$]@mesoporous g-C_3N_4, respectively. Additionally, at the current densities of 6, 5, 4, 3, and 2 A g^{-1}, mesoporous g-C_3N_4 had energy densities of 2.3, 2.5, 2.7, 3.0, and 3.3 Wh kg^{-1}, [4,4′-dmbipy·H]$_2$[$IrCl_6$] had

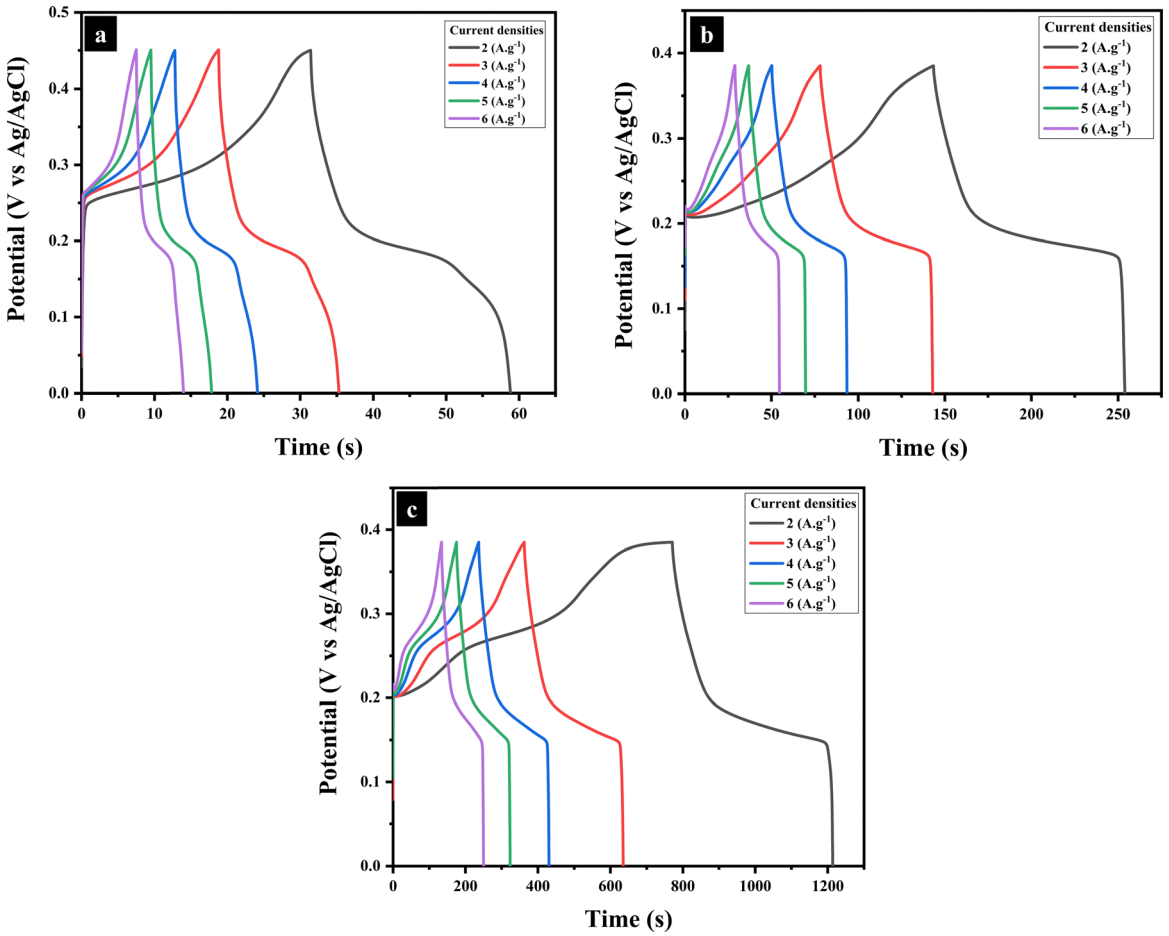

Fig. 8 GCD plots of mesoporous g-C_3N_4 (a), [4,4′-dmbipy·H]$_2$[IrCl$_6$] (b) and [4,4′-dmbipy·H]$_2$[IrCl$_6$]@mesoporous g-C_3N_4 (c).

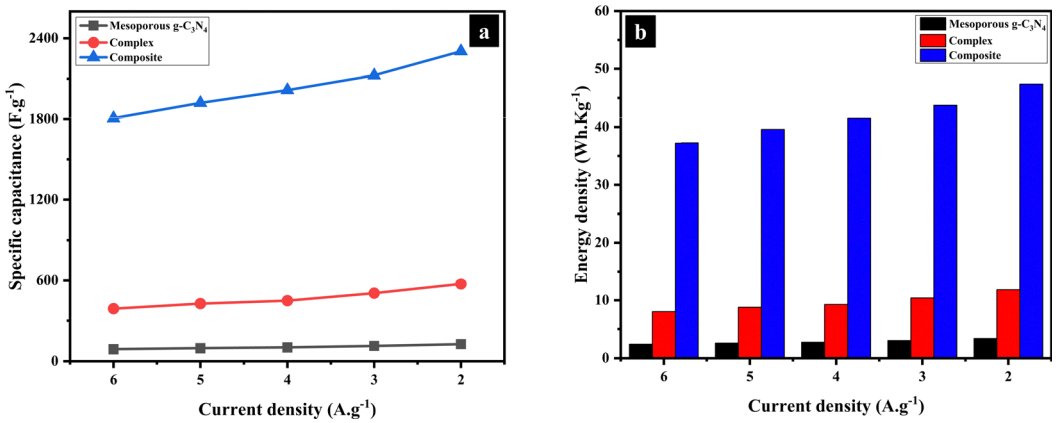

Fig. 9 Comparison of the specific capacitance (a) and energy density (b) of the as-prepared materials at different current densities.

Table 4 Comparison of the power density of the as-prepared materials at different current densities

Materials	Current densities (A g^{-1})				
	2	3	4	5	6
Mesoporous g-C_3N_4	439.85	658.53	858.94	1097.14	1318.15
[4,4′-dmbipy·H]$_2$[IrCl$_6$]	384.73	577.44	769.88	961.82	1154.88
[4,4′-dmbipy·H]$_2$[IrCl$_6$]@mesoporous g-C_3N_4	384.93	577.42	769.91	962.63	1154.79

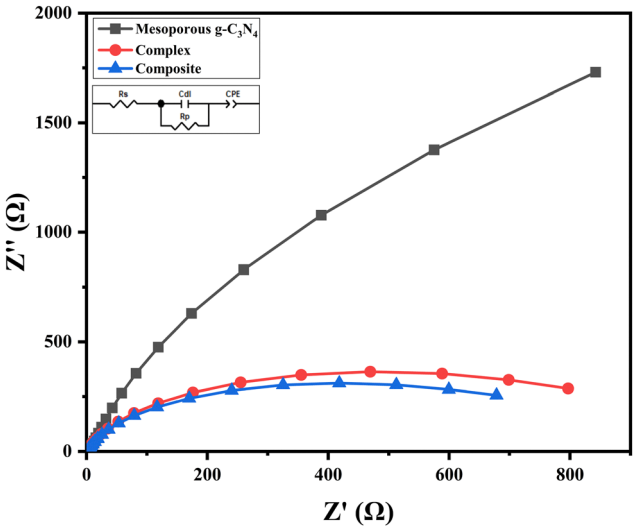

Fig. 10 EIS plots of mesoporous g-C_3N_4, [4,4′-dmbipy·H]$_2$[$IrCl_6$] and [4,4′-dmbipy·H]$_2$[$IrCl_6$]@mesoporous g-C_3N_4.

8.0, 8.7, 9.2, 10.4, and 11.8 Wh kg^{-1}, and [4,4′-dmbipy·H]$_2$[$IrCl_6$]@mesoporous g-C_3N_4 had the best outcomes of 37.2, 39.5, 41.4, 43.7, and 47.3 Wh kg^{-1}, respectively. Finally, the power densities of the as-prepared materials were 1318.1, 1097.1, 858.9, 658.5, and 439.5 W kg^{-1} for mesoporous g-C_3N_4, 1154.8, 961.8, 769.8, 577.4, and 384.7 W kg^{-1} for [4,4′-dmbipy·H]$_2$[$IrCl_6$], and 1154.7, 962.4, 769.9, 577.4, and 384.9 W kg^{-1} for [4,4′-dmbipy·H]$_2$[$IrCl_6$]@mesoporous g-C_3N_4 at current densities of 6, 5, 4, 3, and 2 A g^{-1}, respectively. Notably, the double-peaked characteristic emerging at roughly 0.3 V, as demonstrated by the CV curves of [4,4′-dmbipy·H]$_2$[$IrCl_6$] and [4,4′-dmbipy·H]$_2$[$IrCl_6$]@mesoporous g-C_3N_4, was weakly seen in the GCD plot of [4,4′-dmbipy·H]$_2$[$IrCl_6$], but was clearly visible in the GCD plot of [4,4′-dmbipy·H]$_2$[$IrCl_6$]@mesoporous g-C_3N_4. A comparison of the as-prepared materials in terms of the specific capacitance, energy density, and power density at various current densities is performed in Fig. 9a and b, and Table 4, respectively.

Electrochemical impedance spectroscopy (EIS) measurements were carried out from 100 kHz to 0.1 Hz in order to

Table 5 Fitting results for EIS plots

Materials	R_s	C_{dl}	R_p	CPE-T	CPE-P
Mesoporous g-C_3N_4	0.70	12.09×10^{-4}	2303	17.86×10^{-4}	0.75
[4,4′-dmbipy·H]$_2$[$IrCl_6$]	0.77	6.63×10^{-4}	546.6	53.60×10^{-4}	0.69
[4,4′-dmbipy·H]$_2$[$IrCl_6$]@mesoporous g-C_3N_4	0.72	7.77×10^{-4}	440.8	52.25×10^{-4}	0.67

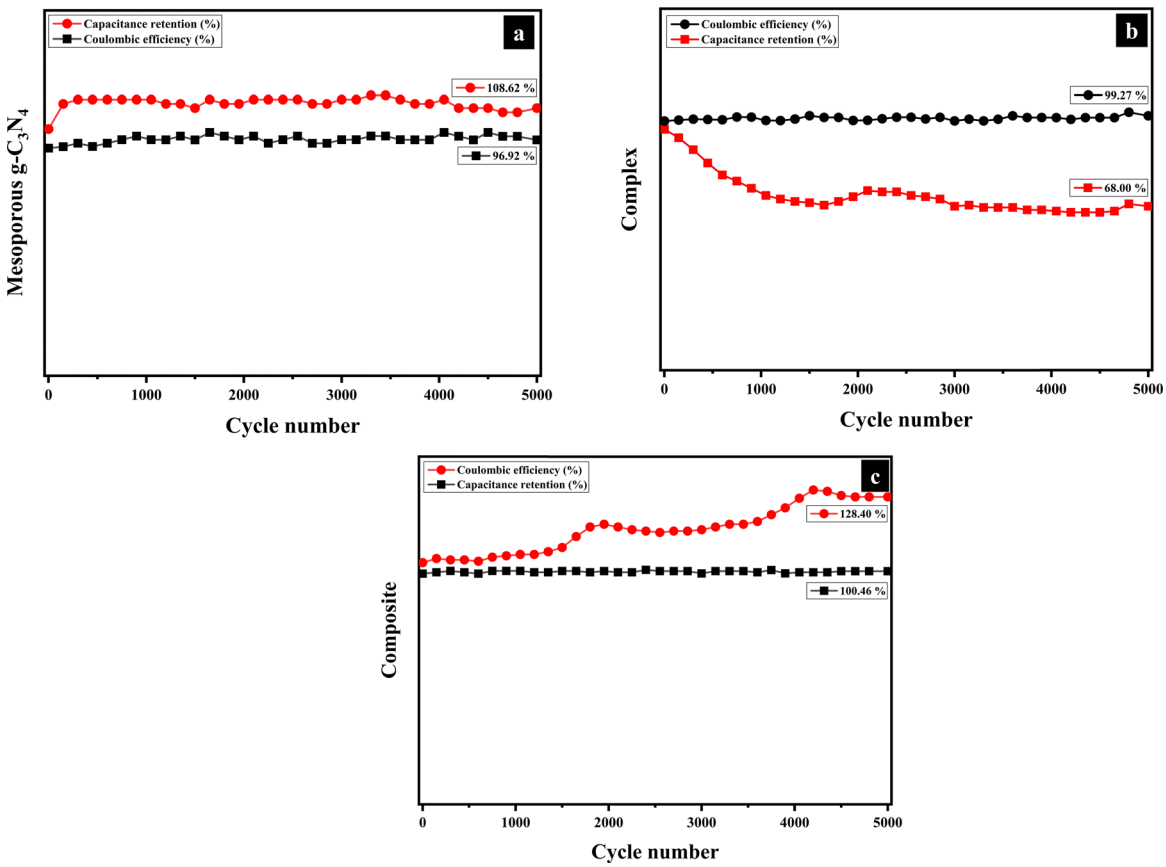

Fig. 11 Stability performance of mesoporous g-C_3N_4 (a), [4,4′-dmbipy·H]$_2$[$IrCl_6$] (b) and [4,4′-dmbipy·H]$_2$[$IrCl_6$]@mesoporous g-C_3N_4 (c).

assess the impedance of the as-prepared materials, as shown in Fig. 10. Additionally, the results of applying the equivalent circuit fit obtained by the Z View software are listed in Table 5. Although mesoporous g-C_3N_4 individually exhibited R_p = 2303 Ω, with C_{dl} = 12.09 × 10^{-4} F and R_s = 0.70 Ω, as demonstrated by the GCD and CV results, the positive and impressive impact of mesoporous g-C_3N_4 was clearly shown in the EIS of the composite by the reduction in the R_s and R_p from 0.77 Ω and 546.6 Ω for [4,4′-dmbipy·H]$_2$[$IrCl_6$] to 0.72 Ω and 440.8 Ω for [4,4′-dmbipy·H]$_2$[$IrCl_6$]@mesoporous g-C_3N_4, in addition to the improvement in the C_{dl} from 6.63 × 10^{-4} F to 7.77 × 10^{-4} F, respectively.

Fig. 11 shows the cycle stability performance of mesoporous g-C_3N_4 (a), [4,4′-dmbipy·H]$_2$[$IrCl_6$] (b), [4,4′-dmbipy·H]$_2$[$IrCl_6$]@mesoporous g-C_3N_4. As expected from a carbon-based material with non-faradaic reactions and fast charge/discharge capabilities, despite its high stability, mesoporous g-C_3N_4 exhibited a 108.62% capacitance retention and a 96.92% Coulombic efficiency after 5000 cycles at a current density of 5 A g^{-1}. Even so, [4,4′-dmbipy·H]$_2$[$IrCl_6$] had a notable Coulombic efficiency (99.27%) after 5000 cycles at a current density of 8 A g^{-1}, but with a 32% less capacitance in proportion with the first cycle, reaching a 68.00% capacitance retention after 5000 cycles, which could be brought on by the Faradic reaction of the complex. Eventually, from CV, GCD, and EIS results, the significant impact of mesoporous g-C_3N_4 on the composite became apparent, with improvement in the capacitance retention of [4,4′-dmbipy·H]$_2$[$IrCl_6$]@mesoporous g-C_3N_4 to 128.40% and a good Coulombic efficiency of 100.46% at a high current density of 20 A g^{-1} after 5000 cycles.

Conclusion

In this study, the [4,4′-dmbipy·H]$_2$[$IrCl_6$] complex and its composite with mesoporous g-C_3N_4 ([4,4′-dmbipy·H]$_2$[$IrCl_6$]@mesoporous g-C_3N_4) were synthesized, and their performance and use in supercapacitors were investigated. The [4,4′-dmbipy·H]$_2$[$IrCl_6$] complex performed satisfactorily by exhibiting a 574 F g^{-1} specific capacitance and a 11.8 Wh kg^{-1} energy density at a current density of 2 A g^{-1}. Because mesoporous g-C_3N_4, a carbon-based material, offered amazing features like high specific surface areas and stability, the electrochemical performance of [4,4′-dmbipy·H]$_2$[$IrCl_6$]@mesoporous g-C_3N_4 was evidently raised, with a specific capacitance of 2302 F g^{-1} and energy density of 47.3 Wh kg^{-1} at the same current density. The cycle stability test of the as-prepared materials showed a Coulombic efficiency of 99.27% for [4,4′-dmbipy·H]$_2$[$IrCl_6$] at a current density of 8 A g^{-1} and a Coulombic efficiency of 100.46% at a high current density of 20 A g^{-1} for [4,4′-dmbipy·H]$_2$[$IrCl_6$]@mesoporous g-C_3N_4. It can be concluded that the practical effects of mesoporous g-C_3N_4 were greatly enhanced by increasing the capacitance retention from 68% for [4,4′-dmbipy·H]$_2$[$IrCl_6$] to 128.40% for [4,4′-dmbipy·H]$_2$[$IrCl_6$]@mesoporous g-C_3N_4.

Conflicts of interest

There are no conflicts to declare.

Data availability

The data supporting this article have been included in the manuscript.

CCDC 2453322 contains the supplementary crystallographic data for this paper.[54]

Acknowledgements

We would like to thank the Iran University of Science and Technology and Farhangian University for their support.

References

1 H. M. Ali, T. Rehman, M. Arıcı, Z. Said, B. Duraković and H. I. Mohammed, *et al.*, Advances in thermal energy storage: Fundamentals and applications, *Prog. Energy Combust. Sci.*, 2024, **100**, 101109, DOI: 10.1016/j.pecs.2023.101109.
2 M. M. Rahman, A. O. Oni, E. Gemechu and A. Kumar, Assessment of energy storage technologies: A review, *Energy Convers. Manag.*, 2020, **223**, 113295, DOI: 10.1016/j.enconman.2020.113295.
3 M. K. G. Deshmukh, M. Sameeroddin, D. Abdul and M. Abdul Sattar, Renewable energy in the 21st century: A review, *Mater. Today Proc.*, 2023, **80**, 1756–1759, DOI: 10.1016/j.matpr.2021.05.501.
4 M. Z. Iqbal and U. Aziz, Supercapattery: Merging of battery-supercapacitor electrodes for hybrid energy storage devices, *J. Energy Storage*, 2022, **46**, 103823, DOI: 10.1016/j.est.2021.103823.
5 S. Karthikeyan, B. Narenthiran, A. Sivanantham, L. D. Bhatlu and T. Maridurai, Supercapacitor: Evolution and review, *Mater Today Proc.*, 2020, 3984–3988, DOI: 10.1016/j.matpr.2021.02.526.
6 A. L. A. Z. Shaqsi, K. Sopian and A. Al-Hinai, Review of energy storage services, applications, limitations, and benefits, *Energy Rep.*, 2020, 288–306, DOI: 10.1016/j.egyr.2020.07.028.
7 F. Naseri, S. Karimi, E. Farjah and E. Schaltz, Supercapacitor management system: A comprehensive review of modeling, estimation, balancing, and protection techniques, *Renewable Sustainable Energy Rev.*, 2022, **111**, 111913, DOI: 10.1016/j.rser.2021.111913.
8 S. Sharma and P. Chand, Supercapacitor and electrochemical techniques: A brief review, *Results Chem.*, 2023, **5**, 100885, DOI: 10.1016/j.rechem.2023.100885.
9 Z. Yan, S. Luo, Q. Li, Z. S. Wu and S. Liu, Recent Advances in Flexible Wearable Supercapacitors: Properties, Fabrication, and Applications, *Adv. Sci.*, 2024, **11**(8), 2302172, DOI: 10.1002/advs.202302172.
10 S. H. S. Pai, A. Sasmal, A. K. Nayak and H. Han, Facile Solvothermal Synthesis of NiO/g-C_3N_4 Nanocomposite for

Enhanced Supercapacitor Application, *Int. J. Energy Res.*, 2023, DOI: 10.1155/2023/1524859.

11 K. Dissanayake and D. Kularatna-Abeywardana, A review of supercapacitors: Materials, technology, challenges, and renewable energy applications, *J. Energy Storage*, 2024, **96**, 112563, DOI: 10.1016/j.est.2024.112563.

12 K. O. Oyedotun, J. O. Ighalo, J. F. Amaku, C. Olisah, A. O. Adeola and K. O. Iwuozor, *et al.*, Advances in Supercapacitor Development: Materials, Processes, and Applications, *J. Electron Mater.*, 2023, 96–129, DOI: 10.1007/s11664-022-09987-9.

13 P. Lamba, P. Singh, P. Singh, P. Singh, Bharti and A. Kumar, *et al.*, Recent advancements in supercapacitors based on different electrode materials: Classifications, synthesis methods and comparative performance, *J. Energy Storage*, 2022, **48**, 103871, DOI: 10.1016/j.est.2021.103871.

14 V. Molahalli, K. C. Singh, M. K. Agrawal, M. Krishnan and S. G. Hegde, Past decade of supercapacitor research – Lessons learned for future innovations, *J. Energy Storage*, 2023, **70**, 108062, DOI: 10.1016/j.est.2023.108062.

15 M. Libber, N. Gariya and M. Kumar, A comprehensive analysis of supercapacitors with current limitations and emerging trends in research, *J. Solid State Electrochem.*, 2025, 513–527, DOI: 10.1007/s10008-024-06107-x.

16 A. B. S. Semente, R. S. Sampaio, T. M. Silva and M. F. Montemor, Electrochemical growth optimization of IrOx films on stainless steel as electrodes for high performance supercapacitors, *Electrochim. Acta*, 2025, 512, DOI: 10.1016/j.electacta.2024.145421.

17 S. A. Beknalkar, A. M. Teli, N. S. Harale, D. S. Patil, S. A. Pawar and J. C. Shin, *et al.*, Fabrication of high energy density supercapacitor device based on hollow iridium oxide nanofibers by single nozzle electrospinning, *Appl. Surf. Sci.*, 2021, 546, DOI: 10.1016/j.apsusc.2021.149102.

18 A. Zaka, M. W. Iqbal, A. K. Alqorashi, B. S. Almutairi and H. Alrobei, Iron-iridium metal organic framework/nitrogen doped MXene/graphene quantum dots: A leading composite for electrolytic energy storage and hydrogen evolution reaction, *Diamond Relat. Mater.*, 2024, **149**, 11653, DOI: 10.1016/j.diamond.2024.111653.

19 S. A. Beknalkar, A. M. Teli, N. S. Harale, J. C. Shin and P. S. Patil, Construction of IrO_2@Mn_3O_4 core-shell heterostructured nanocomposites for high performance symmetric supercapacitor device, *J. Alloys Compd.*, 2021, 887, DOI: 10.1016/j.jallcom.2021.161328.

20 P. Gaikwad, N. Tiwari, R. Kamat, S. M. Mane and S. B. Kulkarni, A comprehensive review on the progress of transition metal oxides materials as a supercapacitor electrode, *Mater. Sci. Eng., B*, 2024, **307**, 117544, DOI: 10.1016/j.mseb.2024.117544.

21 S. V. Sadavar, S. Y. Lee and S. J. Park, Advancements in Asymmetric Supercapacitors: From Historical Milestones to Challenges and Future Directions, *Adv. Sci.*, 2024, **11**(34), 2403172, DOI: 10.1002/advs.202403172.

22 M. A. Dar, S. R. Majid, M. Satgunam, C. Siva, S. Ansari and P. Arusalan, *et al.*, Advancements in Supercapacitor electrodes and perspectives for future energy storage technologies, *Int. J. Hydrogen Energy*, 2024, 10–28, DOI: 10.1016/j.ijhydene.2024.05.191.

23 M. Kandasamy, S. Sahoo, S. K. Nayak, B. Chakraborty and C. S. Rout, Recent advances in engineered metal oxide nanostructures for supercapacitor applications: Experimental and theoretical aspects, *J. Mater. Chem. A*, 2021, 17643–17700, DOI: 10.1039/d1ta03857e.

24 S. Jayakumar, P. C. Santhosh, M. M. Mohideen and A. V. Radhamani, A comprehensive review of metal oxides (RuO_2, Co_3O_4, MnO_2 and NiO) for supercapacitor applications and global market trends, *J. Alloys Compd.*, 2024, **976**, 173170, DOI: 10.1016/j.jallcom.2023.173170.

25 K. Sheoran, H. Kaur, S. S. Siwal and V. K. Thakur, Dual Role is Always Better than Single: Ionic Liquid as a Reaction Media and Electrolyte for Carbon-Based Materials in Supercapacitor Applications, *Adv. Energy Sustainability Res.*, 2023, **4**(9), DOI: 10.1002/aesr.202300021.

26 N. K. Pavithra Siddu, S. M. Jeong and C. S. Rout, MXene-carbon based hybrid materials for supercapacitor applications, *Energy Adv.*, 2024, 341–365, DOI: 10.1039/d3ya00502j.

27 R. Kumar, E. Joanni, S. Sahoo, J. J. Shim, W. K. Tan and A. Matsuda, *et al.*, An overview of recent progress in nanostructured carbon-based supercapacitor electrodes: From zero to bi-dimensional materials, *Carbon*, 2022, 298–338, DOI: 10.1016/j.carbon.2022.03.023.

28 Z. Zhai, L. Zhang, T. Du, B. Ren, Y. Xu and S. Wang, *et al.*, A review of carbon materials for supercapacitors, *Mater Des.*, 2022, **221**, 111017, DOI: 10.1016/j.matdes.2022.111017.

29 T. W. Chen, S. M. Chen, G. Anushya, R. Kannan, P. Veerakumar and A. G. Al-Sehemi, *et al.*, Electrochemical energy storage applications of functionalized carbon-based nanomaterials: An overview, *Int. J. Electrochem. Sci.*, 2024, **19**(5), 100548, DOI: 10.1016/j.ijoes.2024.100548.

30 G. Kothandam, G. Singh, X. Guan, J. M. Lee, K. Ramadass and S. Joseph, *et al.*, Recent Advances in Carbon-Based Electrodes for Energy Storage and Conversion, *Adv. Sci.*, 2023, **10**(18), 2301045, DOI: 10.1002/advs.202301045.

31 S. R. Khaladkar, O. Maurya, G. Gund, B. Sinha, D. Dubal and R. R. Deshmukh, *et al.*, Improving the charge kinetics through in-situ growth of NiSe nanoparticles on g-C_3N_4 nanosheets for efficient hybrid supercapacitors, *J. Energy Chem.*, 2023, **87**, 304–313, DOI: 10.1016/j.jechem.2023.08.048.

32 Y. Chen and C. Lu, Graphitic carbon nitride nanomaterials for high-performance supercapacitors, *Carbon Neutralizat.*, 2023, **2**, 585–602, DOI: 10.1002/cnl2.87.

33 R. Chakraborty, K. Vilya, M. Pradhan and A. K. Nayak, Recent advancement of biomass-derived porous carbon based materials for energy and environmental remediation applications, *J. Mater. Chem. A*, 2022, 6965–7005, DOI: 10.1039/d1ta10269a.

34 S. R. Khaladkar, O. Maurya, G. Gund, B. Sinha, D. Dubal and R. Deshmukh, *et al.*, Extrinsic Pseudocapacitive NiSe/rGO/g-C_3N_4 Nanocomposite for High-Performance Hybrid Supercapacitors, *ACS Appl. Mater. Interfaces*, 2024, **16**, 11408–11420, DOI: 10.1021/acsami.3c16010.

35 A. Meftahi, M. Shabani-Nooshabadi and A. Reisi-Vanani, AgI/g-C_3N_4 nanocomposite as electrode material for supercapacitors: Comparative study for its efficiency in three different aqueous electrolytes, *Electrochim. Acta.*, 2022, **430**, 141052, DOI: 10.1016/j.electacta.2022.141052.

36 Z. S. Rozveh, M. Moradi, M. Keyhan, V. Safarifard, P. Yaghoubizadeh and M. J. Eshraghi, The electrochemical performance of gallium nitride composited with g-C_3N_4 in bulk and oxidized forms for supercapacitors, *Synth. Methods*, 2024, **307**, 117686, DOI: 10.1016/j.synthmet.2024.117686.

37 S. Khasim, A. Pasha, M. Lakshmi, C. Panneerselvam, M. F. Ullah and A. A. A. Darwish, *et al.*, Synthesis of g-C_3N_4/CuO Nanocomposite as a Supercapacitor with Improved Electrochemical Performance for Energy Storage applications, *Int. J. Electrochem. Sci.*, 2022, **17**(8), 220838, DOI: 10.20964/2022.08.29.

38 T. Zahra, I. Barsoum, F. F. Alharbi, Z. Ahmad, H. H. Somaily and M. Abdullah, *et al.*, Fabrication of V_2O_5@g-C_3N_4 nanocomposite by hydrothermal route for use as an improved electrochemical property in supercapacitor applications, *J. Energy Storage*, 2024, **87**, 111470, DOI: 10.1016/j.est.2024.111470.

39 C. Sandoval-Pauker, G. Molina-Aguirre and B. Pinter, Status report on copper (I) complexes in photoredox catalysis; photophysical and electrochemical properties and future prospects, *Polyhedron*, 2021, 199, DOI: 10.1016/j.poly.2021.115105.

40 D. Ma, T. Tsuboi, Y. Qiu and L. Duan, Recent Progress in Ionic Iridium(III) Complexes for Organic Electronic Devices, *Adv. Mater.*, 2017, **29**(3), 1603253, DOI: 10.1002/adma.201603253.

41 Y. Huang, L. Yang, W. Huang, J. Li, C. Liu and B. Lai, *et al.*, Mesoporous tubular g-C_3N_4 as an efficient metal-free photocatalyst with peroxymonosulfate to degrade carbamazepine, *J. Hazard. Mater. Lett.*, 2023, **4**, 100081, DOI: 10.1016/j.hazl.2023.100081.

42 E. Jamshidi, S. Dalvand, F. Manteghi and S. M. Mousavi-Khoshdel, A cobalt-aluminium layered double hydroxide with a nickel core-shell structure nanocomposite for supercapacitor applications, *iScience*, 2025, **28**, 111672, DOI: 10.1016/j.isci.2024.111672.

43 S. Mohammadi, A. M. Homayounfard and S. M. Mousavi-Khoshdel, High-Performance Ni(II)@Amine-Functionalized Graphene Oxide Composite as Supercapacitor Electrode: Theoretical and Experimental Study, *ACS Appl. Energy Mater.*, 2024, **7**, 6142–6154, DOI: 10.1021/acsaem.4c00564.

44 Y. Guan, J. Wu, L. Wang, C. H. Shi, K. Lv and Y. Lv, Application of g-C_3N_4/CNTs nanocomposites in energy and environment, *Energy Rep.*, 2022, **8**, 1190–1199, DOI: 10.1016/j.egyr.2022.02.081.

45 M. Zhang, N. Han, Y. Fei, J. Liu, L. Xing and A. Núñez-Delgado, *et al.*, TiO_2/g-C_3N_4 photocatalyst for the purification of potassium butyl xanthate in mineral processing wastewater, *J. Environ. Manage.*, 2021, **297**, 113311, DOI: 10.1016/j.jenvman.2021.113311.

46 S. M. Hosseini and V. Safarifard, A novel PVDF film containing g-C_3N_4@MOF composite for efficient photoreduction of Cr(VI) under visible light, *Surf. Interfaces*, 2024, 55, DOI: 10.1016/j.surfin.2024.105399.

47 S. Nasser Ostad, A. Abedi, V. Amani, P. Karimi and S. Heydarnezhad, Influence of methyl group position in bipyridine ligand on structure and luminescence of related zinc(II) nitrate complexes, *J. Iran. Chem. Soc.*, 2016, **13**, 1417–1427, DOI: 10.1007/s13738-016-0857-3.

48 V. Amani, A. Abedi, S. Ghabeshi, H. R. Khavasi, S. M. Hosseini and N. Safari, Synthesis and characterization of a series of gold(III) complexes with the 4,4′-dimethyl-2,2′-bipyridine ligand: Counterion influence on the cytotoxicity of gold(III) complexes, *Polyhedron*, 2014, **79**, 104–115, DOI: 10.1016/j.poly.2014.04.064.

49 V. Amani, N. Safari and H. R. Khavasi, Akkurt M. Synthesis, characterization and crystal structure determination of platinum(IV) complexes containing, bipyridine derivatives and chloride, [Pt(5,5′-dmbipy)Cl4] and [Pt(6-mbipy)Cl4], *Polyhedron*, 2009, **28**, 3026–3030, DOI: 10.1016/j.poly.2009.06.053.

50 V. Amani and R. Tayebee, Synthesis, characterization, thermal analyses and crystal structure of a new Thorium(IV) nitrate complex: $[phen.H]_2[Th(NO_3)_6]$ $2H_2O$, *Synth. React. Inorg., Met.-Org., Nano-Met. Chem.*, 2013, **43**, 1118–1123, DOI: 10.1080/15533174.2012.756025.

51 V. Amani, N. Safari, H. R. Khavasi and P. Mirzaei, Iron(III) mixed-ligand complexes: Synthesis, characterization and crystal structure determination of iron(III) hetero-ligand complexes containing 1,10-phenanthroline, 2,2′-bipyridine, chloride and dimethyl sulfoxide, [Fe(phen)Cl3(DMSO)] and [Fe(bipy)Cl3(DMSO)], *Polyhedron*, 2007, **26**, 4908–4914, DOI: 10.1016/j.poly.2007.06.038.

52 V. Amani, N. Safari and H. R. Khavasi, Synthesis, characterization and crystal structure determination of iron(III) hetero-ligand complexes containing 2,2′-bipyridine, 5,5′-dimethyl-2,2′-bipyridine and chloride, $[Fe(bipy)Cl_4][bipy{\cdot}H]$ and $[Fe(dmbipy)_2Cl_2][FeCl_4]$, *Polyhedron*, 2007, **26**, 4257–4262, DOI: 10.1016/j.poly.2007.05.050.

53 A. K. Nayak and T. Gopalakrishnan, Phase- and Crystal Structure-Controlled Synthesis of Bi_2O_3, Fe_2O_3, and $BiFeO_3$ Nanomaterials for Energy Storage Devices, *ACS Appl. Nano Mater.*, 2022, **5**, 14663–14676, DOI: 10.1021/acsanm.2c03026.

54 CCDC 2453322: Experimental Crystal Structure Determination, 2025, DOI: 10.5517/ccdc.csd.cc2nbwfb.